Bi- and trilayer graphene solutions

Chih-Jen Shih[1], Aravind Vijayaraghavan[1,2], Rajasekar Krishnan[1], Richa Sharma[1], Jae-Hee Han[1,3], Moon-Ho Ham[1], Zhong Jin[1], Shangchao Lin[1,4], Geraldine L.C. Paulus[1], Nigel Forest Reuel[1], Qing Hua Wang[1], Daniel Blankschtein[1] and Michael S. Strano[1]*

Bilayer and trilayer graphene with controlled stacking is emerging as one of the most promising candidates for post-silicon nanoelectronics. However, it is not yet possible to produce large quantities of bilayer or trilayer graphene with controlled stacking, as is required for many applications. Here, we demonstrate a solution-phase technique for the production of large-area, bilayer or trilayer graphene from graphite, with controlled stacking. The ionic compounds iodine chloride (ICl) or iodine bromide (IBr) intercalate the graphite starting material at every second or third layer, creating second- or third-stage controlled graphite intercalation compounds, respectively. The resulting solution dispersions are specifically enriched with bilayer or trilayer graphene, respectively. Because the process requires only mild sonication, it produces graphene flakes with areas as large as 50 μm^2. Moreover, the electronic properties of the flakes are superior to those achieved with other solution-based methods; for example, unannealed samples have resistivities as low as $\sim$1 kΩ and hole mobilities as high as $\sim$400 cm^2 V^{-1} s^{-1}. The solution-based process is expected to allow high-throughput production, functionalization, and the transfer of samples to arbitrary substrates.

Graphene, with sheets consisting of fewer than 10 stacked layers of sp^2-hybridized carbon lattice[1], combines outstanding electronic and mechanical properties[2–4]. Owing to their distinct electronic band structures, AB-stacked bilayer[2,3,5] and trilayer[4] graphene have extraordinary potential for next-generation optoelectronic and microprocessor applications. However, these promising materials require the development of new synthesis methods to effectively control the number of AB-stacked layers by means of graphite exfoliation and processing. There has been substantial progress in the production of graphene through the micromechanical cleavage of mono- and few-layer graphene[6] from highly-ordered pyrolytic graphite (HOPG). However, this approach lacks a viable mechanism for scalable manufacturing. Epitaxial growth on an SiC substrate[7] provides advantages in this respect, but imposes constraints on the choice of substrate. Recent results have demonstrated chemical vapour deposition (CVD) for graphene growth and transfer to various substrates[8–10]. However, for bi- or tri-layer applications, SiC and CVD graphene films tend to be turbostratic, where slight deviation from the AB stacking destroys the unique electronic structures of the bilayer and trilayer graphene, making it electronically similar to monolayer graphene[11,12]. Alternatively, exfoliation of pristine graphite into a liquid phase is easily scalable and allows for more precise chemical modification in solution[13,14]. If layering can be controlled during dissolution, this would provide a viable route for the mass production of AB-stacked bi- and few-layer graphene on arbitrary substrates for electronic devices. The liquid-phase production of chemically converted graphene from graphene oxide (GO) is a high-yield method for monolayer graphene-based solutions[15–19]. Despite producing high-concentration dispersions with large flake areas, a substantial number of defects are introduced during the reduction process[20,21], and the intrinsic properties of graphene are only partially restored[22]. Liquid-phase exfoliation of graphite in organic solvents[23–25] and surfactant aqueous solutions[26,27] are promising routes to the production of pristine graphene dispersions. To date,

however, they all share the limitation that the produced flakes have dimensions less than those suitable for conventional photo-lithography, a manufacturing method for economical mass production[22–27]. Both GO and direct-exfoliation methods also lack direct control over the layering and stacking of the exfoliated flakes[28]. In contrast, when combined with the well-developed inter-calation chemistry of graphite[29,30], it becomes possible to obtain large-size graphene dispersions with layering control. Graphene sheets from covalent graphite intercalation compounds (GIC)[31–33], ionic GIC[34–36] and expanded graphite[37] have been reported. Nevertheless, the produced graphene is found to be either significantly defective following the intercalation–expansion process[31–33] or remains too small in area for scalable applications[34,35]. In addition, all liquid-phase methods can only produce size- and layer-polydispersed graphene[28,38]. In the present Article, we demonstrate an important link between the stage number of a non-covalent, precursor GIC and the resulting mode in the layer number dispersion of the resulting exfoliated solution, allowing for solutions enriched in bi- and trilayer graphene. The efficiency of the approach is such that a milder ultrasonic processing is sufficient, so larger flake sizes are recovered, enabling devices produced by conventional photolithography.

Stage-controlled intercalation

HOPG was chosen as a high-quality graphite source, and we used the halogen intercalants ICl (to form Stage-2 ionic GIC) and IBr (to form Stage-3 ionic GIC). The staging phenomenon is related to the effect of long-range lattice strain[29]. Once the exposed surface graphite planes have interacted with the intercalated species, the intercalant molecules are introduced into the host material from the exposed end surfaces, and sequentially form layered structures. In this scheme, Stage-2 and Stage-3 GICs have every second or third layer of the graphite lattice intercalated, respectively[30], as shown in Fig. 1a. The detailed intercalation method is described in Supplementary Section S1. The stage of

[1]Department of Chemical Engineering, Massachusetts Institute of Technology, Cambridge, Massachusetts 02139, USA, [2]School of Computer Science, The University of Manchester, Manchester M13 9PL, UK, [3]Department of Energy IT, Kyungwon University, Seongnam, Gyeonggi-do 461-701, South Korea, [4]Department of Mechanical Engineering, Massachusetts Institute of Technology, Cambridge, Massachusetts 02139, USA. *e-mail: strano@mit.edu
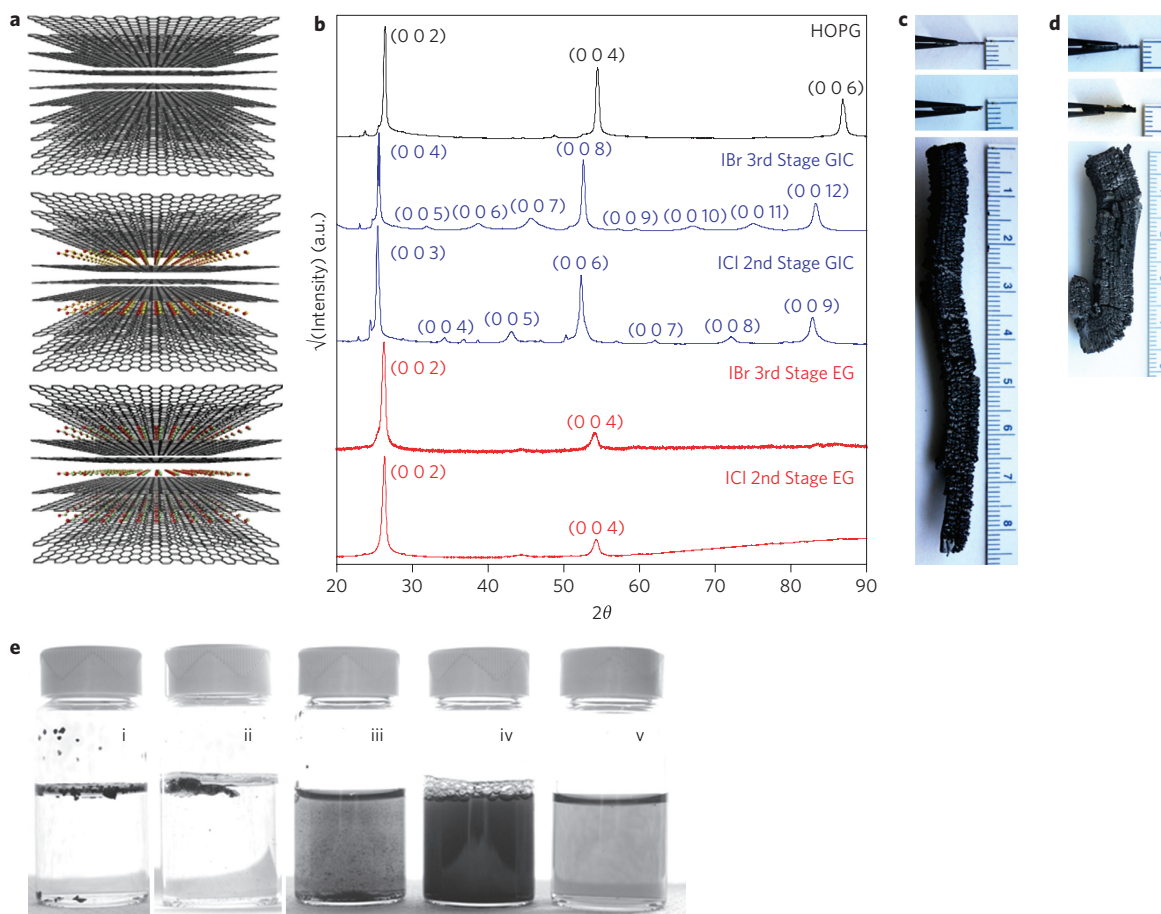
Figure 1 | Graphene dispersions from ionic graphite intercalation compounds (GIC). a, Three-dimensional computer-generated molecular models (carbon, grey; iodine, red; bromine, yellow; chlorine, cyan) of HOPG (top), IBr Stage-3 GIC (middle) and ICl Stage-2 GIC (bottom). **b**, Comparison of XRD patterns of HOPG, IBr Stage-3 GIC, ICl Stage-2 GIC, IBr Stage-3 expanded graphite (EG) and ICl Stage-2 EG. For IBr Stage-3 GIC, an additional three peaks appear between two of the three main peaks corresponding to the (0 0 2), (0 0 4) and (0 0 6) planes in HOPG, which is a clear signature of Stage-3 GIC (the intercalant layer inserts between every three graphite layers). Analogous XRD patterns also apply to the ICl Stage-2 GIC. Both Stage-3 and Stage-2 expanded graphites show much weaker (0 0 4) peaks than the HOPG, while the (0 0 6) peak becomes unobservable. **c**, Photographs of HOPG (top), Stage-3 GIC (middle) and Stage-3 EG (bottom) (the HOPG and GIC materials are held up with tweezers with the edges toward the viewer). **d**, Photographs of HOPG (top), Stage-2 GIC (middle), and Stage-2 EG (bottom). **e**, Photograph of steps involved in forming suspensions of EGs in 2 wt% sodium cholate aqueous solution. As-prepared Stage-3 (i) and Stage-2 (ii) expanded materials floating on the solution, followed by 30 min homogenization (iii) and 10 min sonication (iv). (v) Clear and grey graphene solutions after 2,000 r.p.m. centrifugation.

the GIC denotes the crystallographic arrangement of intercalant and graphite layers, with a superlattice structure confirmed by X-ray diffraction (XRD) patterns along the c-axis[39]. The top three profiles in Fig. 1b illustrate the XRD patterns of HOPG, IBr Stage-3 GIC and ICl Stage-2 GIC, respectively. The crystallographic evidence (Supplementary Section S2) confirms that halogen molecules intercalate every three and two graphite layers.

According to the XRD analysis, it should be noted here that the intercalant peaks in the GIC superlattice exhibit reduced intensities and peak broadenings compared to perfect superlattice crystals[39]. This suggests that the synthesized Stage-2 GIC is dominated by a bilayer superlattice structure, but includes minority crystal phases (including graphite and GIC sub-domains). In addition, the lateral non-uniformity of grain sizes, which is described by the Daumas–Hérold model[40], also plays an important role. These imperfections arise partly because of the fact that the intercalation process is not completely optimized[29], and partly because of the polycrystalline nature of the HOPG. Better control of the intercalation kinetics[29] is currently under investigation with a view towards achieving 100% intercalation to the desired stage.

The obtained Stage-2 and Stage-3 GICs were then used as precursors of expanded graphite. Briefly, the GICs were annealed at 800 °C for 5 min under an argon atmosphere. The IBr or ICl intercalants between the graphene layers were volatilized rapidly and removed completely during the 'thermal shock' process[41]. The substantial, anisotropic volume changes for Stage-3 and Stage-2 expanded samples are shown in Fig. 1c,d, respectively. During the thermal expansion, the bilayer and trilayer crystal domains are isolated and crosslinked by grain boundaries with stacking faults formed during the intercalation process. It is also expected that small sub-domains may collapse and recombine to form thicker, larger crystallites. The symmetry-breaking of the graphite lattice for Stage-3 and Stage-2 expanded materials is shown in the XRD analysis in the bottom two profiles in Fig. 1b. The peak positions corresponding to the (0 0 2) and (0 0 4) planes are almost identical to those in HOPG. This indicates that the intercalant layers are removed and the graphite lattice parameters restored. However, the relative intensity of the (0 0 4) peak is decreased from the HOPG case, and no (0 0 6) peak is observed for either expanded sample. Hence, the sublattices in both materials consist of fewer than four graphite layers, with long-range order greater than
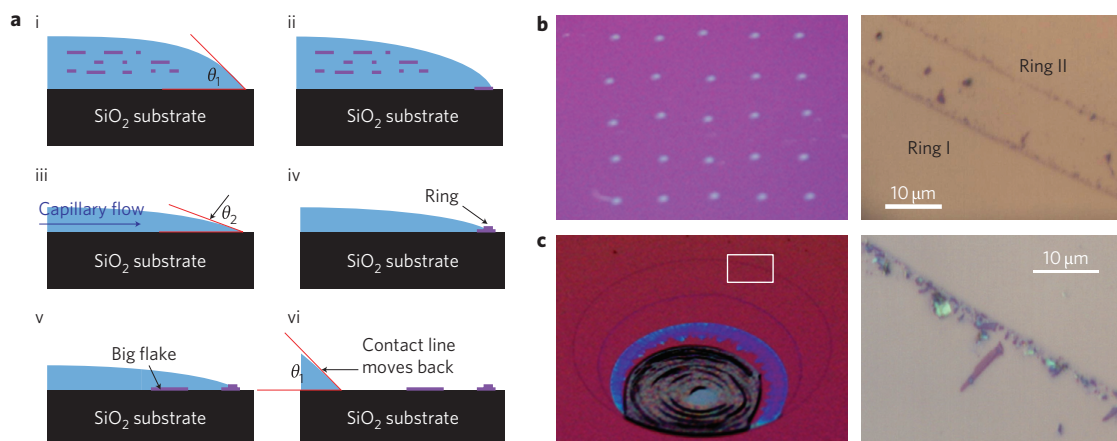
Figure 2 | On-chip separation method based on graphene size, using the 'coffee-ring effect'. a, Schematic of the separation process. (i) A droplet of graphene dispersion on the SiO$_2$ substrate with contact angle θ_1. (ii) Because the evaporation rate is greatest at the drop edge, some graphene flakes deposit along the edge of the drop at the beginning. The presence of these flakes facilitates pinning of the contact line at the drop edge. (iii) The outward capillary flow of liquid is induced from the bulk of the drop, and the contact angle θ_2 becomes gradually smaller. (iv) The liquid flow carries graphene flakes out towards the edge of the drop, which results in the formation of a 'coffee ring'. (v) By controlling the rate of evaporation, all small flakes collect together to form the coffee ring, and particularly large flakes are found inside the coffee ring. (vi) When the contact angle θ_2 becomes too small, the contact line moves back and a smaller droplet forms with contact angle θ_1 again. **b**, Low- (left) and high- (right) magnification images of a matrix of small graphene solution droplets (50 nl each) on a SiO$_2$ wafer, spaced by 4 mm, using a microprinter. Bright dots are associated with surfactant residues after drying. **c**, Low- (left) and high- (right) magnification images of the 'coffee ring'.
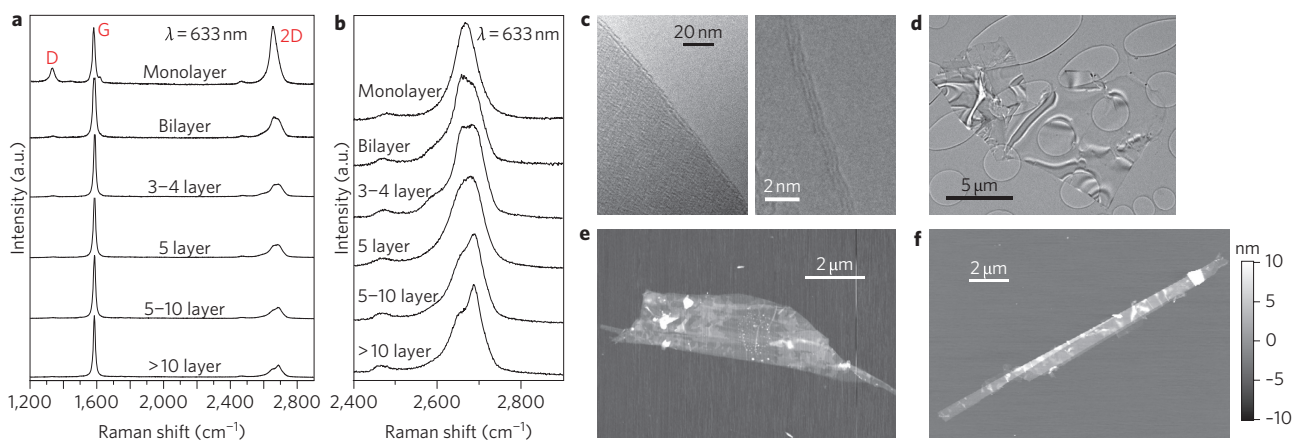

Figure 3 | Characterization of graphene flakes. a,b, Raman spectra (excitation wavelength $\lambda = 633$ nm) for graphene flakes with different numbers of stacked layers. Note that for multilayer graphene flakes, the D-peaks (1,340 cm^{-1}, **a**) are absent, but for the relatively smaller monolayer graphene flake, the weak D-peak arises due to edge effects. 2D Raman spectra (**b**) corresponding to specific numbers of stacked layers of our graphene flakes show the same features observed using the Scotch-tape method on the same substrate. **c**, HRTEM images of the edges of bilayer (left) and trilayer (right) graphene flakes. **d**, TEM image of a representative multilayer graphene flake (area, ~50 μm^2). **e,f**, Representative AFM images of bilayer (**e**) and ~3-4-layer graphene flakes (**f**).

six-layer almost completely absent. Note that, compared with natural graphite, in which the graphene layers are strongly bound by van der Waals interactions, the systematic crystalline defects that crosslink bilayer and trilayer crystallites in expanded materials should be far easier to break up in a liquid-phase dispersion by mild ultrasonication. This also provides a link between the GIC stage number and layer number dispersion in the resulting solution, and hence a route to bi- and trilayer solutions.

Size separation of graphene flakes

The dispersion process for expanded graphite is shown in Fig. 1e. Detailed materials and methods associated with the dispersion process are described in Supplementary Section S3. The main purpose of homogenization is to disassemble weak crosslinks

between crystallites and expel argon gas trapped inside voids. This pretreatment process is required, because ultrasonication is only effective for dispersions inside the liquid, although we expect that the agitation will result in some degree of recombination and aggregation of crystallites in expanded graphite. The protocol of ultrasonication implemented here involves significantly lower strength compared to direct sonication of graphite[24,27]. This appears to preserve large flakes areas in the work reported here. Sonication conditions that are too mild result in ineffective exfoliation of crosslinked defects, so most of the material pellets during centrifugation (the yield is estimated as 3.0%; Supplementary Section S3).

To locate and isolate large flakes from graphene solutions for further characterization, an on-chip separation method based on size using the 'coffee-ring effect'[42–44] was developed. A schematic
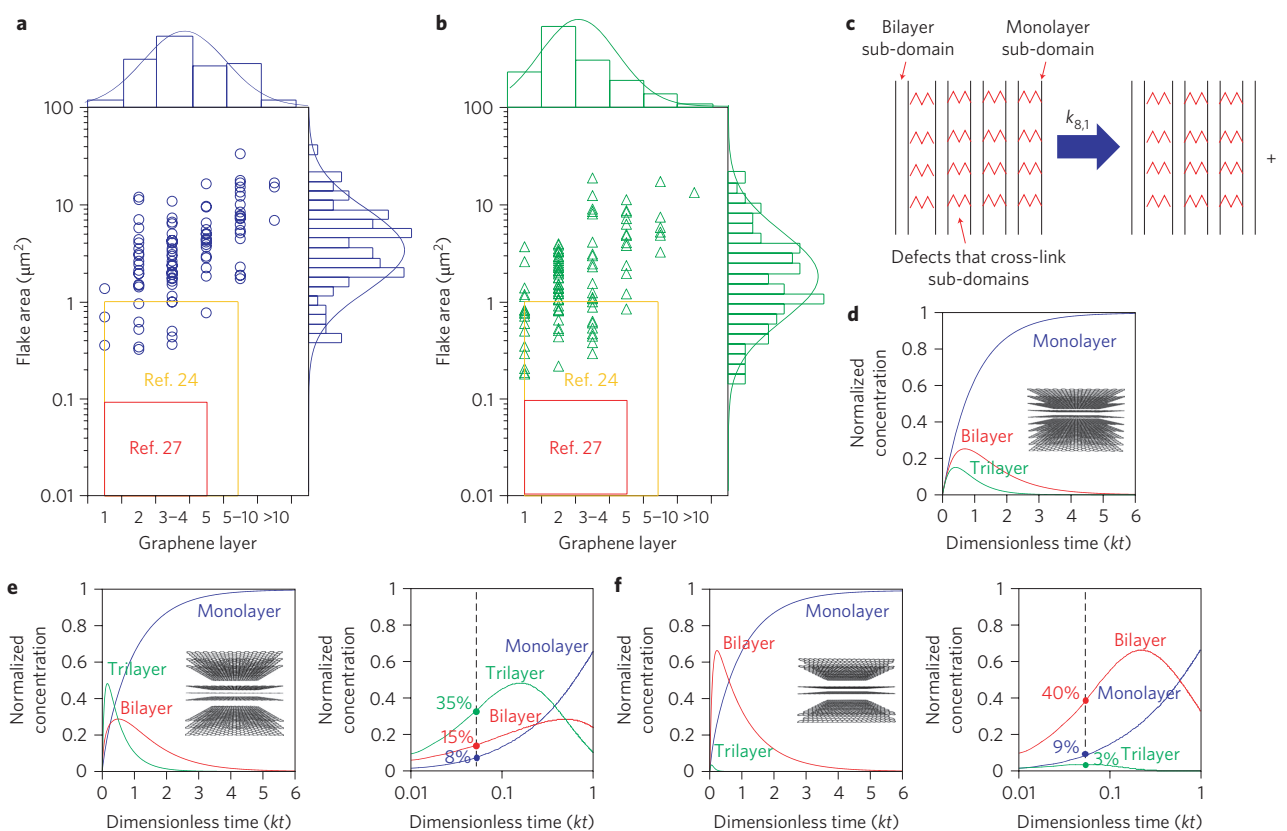
Figure 4 | Evidence for layer- and size-controlled graphene dispersions from different GICs. Distributions for number of stacked layers and the area of graphene flakes inside 'coffee rings' from IBr Stage-3 (**a**) and ICl Stage-2 (**b**) GICs. Regions occupied by graphene solutions produced from direct exfoliation of natural graphite[24,27] are also shown for comparison. **c**, Schematic describing the exfoliation process of a 9-layer graphite lattice into 8- and 1-layer products with rate constant $k_{8,1}$ for a Stage-2 EG system. **d**, Calculated concentrations of mono- (blue curve), bi- (red curve) and tri- (green curve) layer graphene dispersions as a function of dimensionless time using graphite with all interlayer bond strengths equal. **e**, Calculated concentrations for Stage-3 EG with every third interlayer bonds weaker. Adjacent graph shows the predicted time (vertical line) corresponding to the experimentally observed layer distribution for Stage-3 solutions. **f**, Calculated concentrations for Stage-2 EG with every third interlayer bond weaker. Adjacent graph shows the predicted time (vertical line) corresponding to the experimentally observed layer distribution for Stage-2 solutions.

illustration of the mechanism is shown in Fig. 2a. In the formation of size-sorted graphene rings using the coffee-ring effect, the size of the droplet, the concentration of graphene and the substrate temperature all play important roles[45,46]. The optimized process is described in Supplementary Section S4. The on-chip separation method can be further scaled up by (i) increasing the concentration of graphene and (ii) using micro/nanoprinting technology. To demonstrate this, a matrix of graphene droplets (50 nl each) with a droplet spacing of 4 mm was deposited onto a SiO_2–Si substrate using a microprinter, as shown in Fig. 2b. During the evaporation process, ~3–4 rings form for each drop and, in the end, residual surfactant segregates in the central region, which can be rinsed away using deionized water, as shown in Fig. 2c (left image). The larger flakes in the solution can then be found inside each ring, which is composed of the smaller flakes. We also noticed that the proposed method can self-align graphene ribbons along the radial direction of the ring (right image in Fig. 2c).

Evidence for layer-controlled graphene dispersions

Raman spectroscopy was used to characterize the isolated graphene flakes. The full Raman spectra and 2D peaks for representative graphene flakes are shown in Fig. 3a,b, respectively. The 2D peaks corresponding to specific numbers of stacked layers in our exfoliated graphene flakes exhibit the same layering dependence as that observed in micromechanically cleaved graphene on the same substrate[47,48], indicating that the solution-processed graphene flakes are

AB stacked. For the monolayer graphene, a single Lorentzian at 2,660 cm^{-1} is seen, and with increasing number of layers, the other spectral component at 2,690 cm^{-1} gradually dominates. The flakes were categorized as monolayer, bilayer, ~3–4-layer, 5-layer, ~5–10-layer and >10-layer graphene after comparing the obtained Raman 2D peak shapes with those in the literature[47,48]. It is desirable to quantify the trilayer graphene yield from the Stage-3 GIC. However, the 2D signature in Raman spectroscopy is unable to unambiguously distinguish 3- and 4-layer graphene. It can only distinguish 3- or 4-layer flakes from bilayer and 5-layer flakes, and this fact should be recognized during the analysis of flake-thickness distribution discussed below. The D-peak (~1,340 cm^{-1}), which is a measure of defects and chemical functionalization, is absent except in monolayer graphene flakes. We note that the monolayers observed are significantly smaller than the bilayer and thicker flakes, and that the D-peak in monolayers results from symmetry-breaking at the edges[47], because the laser spot is the same size as the flake area and includes the flake edges as well as the interior. The exfoliated graphene retains its pristine structure and does not contain significant defects or functionalization as a result of the intercalation, expansion or solution processing. Additional Raman analysis is presented in Supplementary Figs S7 and S8.

Large graphene flakes can also easily be found on a transmission electron microscopy (TEM) grid. Figure 3c shows high-resolution TEM (HRTEM) images of edges of bilayer and trilayer flakes. Figure 3d shows a TEM image of a representative few-layer graphene
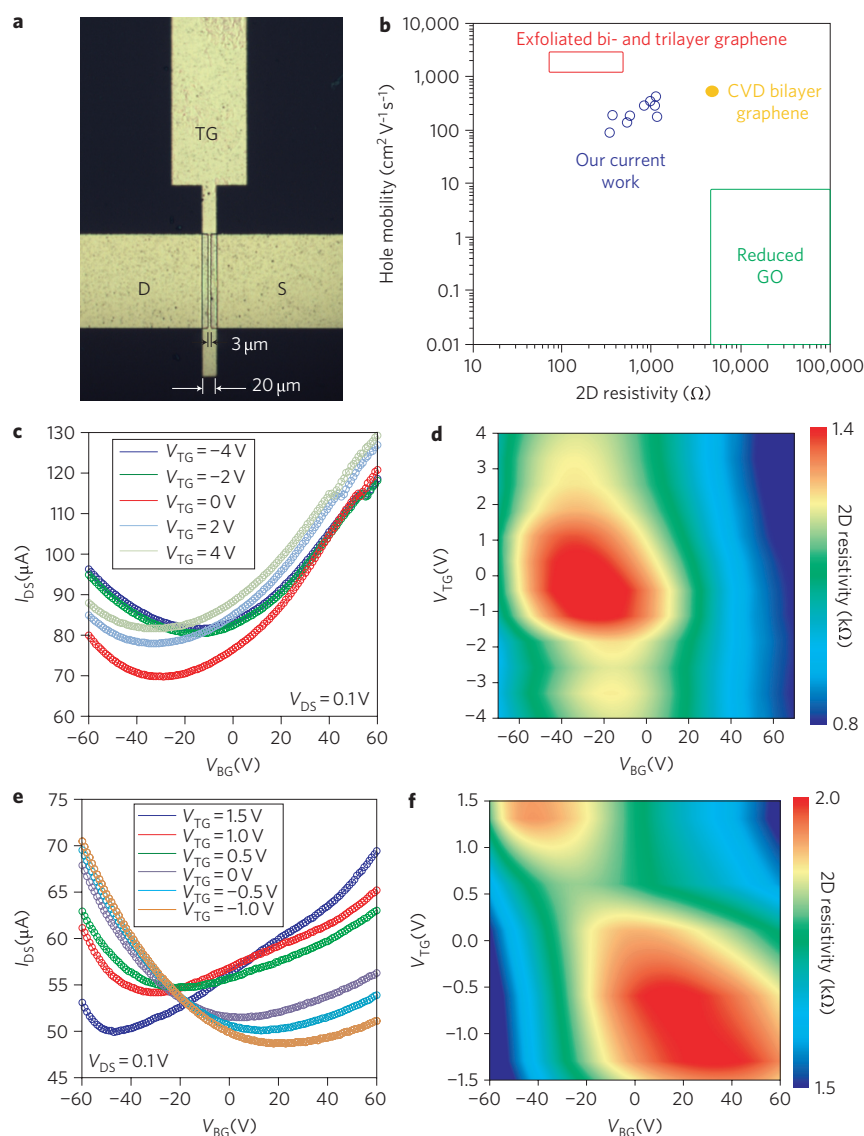
Figure 5 | Electronic characteristics of bilayer and ~3–4-layer graphene devices in the presence of a perpendicular electric field at room temperature.
a, Low-magnification image of our fabricated top-gate (TG) device on a specific graphene flake. **b**, 2D resistivities and hole mobilities for several unannealed FET devices using our bilayer- or trilayer-enriched graphene dispersions. Reported values corresponding to micromechanically exfoliated bi- and trilayer graphene[52], CVD bilayer graphene[10] and reduced graphene oxide[18,51,53,54] are also shown for comparison. **c,d**, Transfer currents (**c**) and 2D resistivity (**d**) as functions of top-gate voltage (V_{TG}) and bottom-gate voltage (V_{BG}) of a representative ~3–4-layer graphene device. **e,f**, Transfer currents (**e**) and 2D resistivity (**f**) as functions of V_{TG} and V_{BG} of a representative bilayer graphene device.

with an area of ~50 μm^2. Electron diffraction patterns in Supplementary Fig. S4 show typical Bragg reflection intensity ratios[24] for monolayer (Supplementary Fig. S4a) and few-layer (Supplementary Fig. S4b) graphene. Additional TEM images of large few-layer graphene (>10 μm^2) are shown in Supplementary Fig. S5. An HRTEM image of the edge of a monolayer flake is shown in Supplementary Fig. S6. Atomic force microscopy (AFM) images of the isolated bilayer and ~3–4-layer graphene flakes are shown in Fig. 3e,f, respectively. The number of stacked layers was confirmed by *in situ* Raman spectroscopy (Supplementary Figs S9 and S10).

Systematic statistical analysis of size and thickness distributions for graphene flakes inside concentric rings was carried out by a combination of optical microscopy and Raman spectroscopy. Figure 4a,b shows the distributions of graphene flakes from IBr Stage-3 and ICl Stage-2 GICs, respectively. Distributions with modes centred at bilayer flakes (40%) and 3–4-layer flakes (35%) were obtained for Stage-2 and Stage-3 expanded graphite, respectively. This indicates

that we successfully produced layer-controlled, AB-stacked graphene dispersions. For comparison, we have indicated the regions occupied by graphene solutions produced from direct processing of natural graphite[24,27]. Another important feature of the distributions produced in this work is that the flake area increases as the layer number increases, with few-layer graphene flakes being an order of magnitude larger than monolayers. It is clear that the preponderance of bilayer or trilayer graphene flakes in solution corresponds to Stage-2 or Stage-3 superlattice sub-domains created during the intercalation process. Relatively thick flakes are generated either from higher-stage sub-domains in GICs or due to the recombination between crystallites during post-expansion and homogenization processes. Alternatively, small monolayer flakes appear to be exfoliated from larger bilayer and trilayer flakes because ultrasonication was applied. We believe that further optimization of the intercalation process towards 100% Stage-2 or Stage-3 GIC would further narrow the layer size distribution around the desired number of layers. It is also noteworthy that the

method reported here may also be extended to monolayer graphene exfoliation by carrying out Stage-1 intercalation with ICl[49].

The kinetics of the exfoliation and dispersion of graphite materials in the liquid phase using the ultrasonication process is analogous to polymer decomposition[50]. Consider a solution containing graphite (graphene) materials, P_i, which has an i-layer ($1 \leq i \leq m$, where m is the maximum layer number considered) structure. For all possible layer numbers i, the generation rate of the i-layer graphene in the sonication process can be written as

$$\frac{d[P_i]}{dt} = \sum_{j=i+1}^{m} k_{i,j-i}[P_j] - \sum_{j=1}^{i-1} k_{j,i-j}[P_i] \qquad (1)$$

where $[P_i]$ denotes the concentration of P_i. Details of the kinetic model and numerical solutions can be found in Supplementary Section S7. Using natural graphite as the raw material, the 'exfoliation rate constant' can be considered independent of the layer number (that is, $k_{i,j} = k$). In this limit, the layer distribution of exfoliated products remains broad[13], with increasing sonication time biasing the distribution towards monolayer[27] instead of terminating at any specific layer number. The simulated concentrations as a function of time (Fig. 4d) show that the bilayer or trilayer graphene will never dominate. On the other hand, considering the Stage-3 and Stage-2 starting materials, it follows that the exfoliation should be easier for every three and two layers in the materials, respectively. We simulate this by increasing the rate constants for every three (Stage-3) or two (Stage-2) layers by a factor of 10, say; the simulated concentrations as a function of dimensionless time are shown in Fig. 4e,f, respectively. In this scheme, the $k_{8,1}$ rate constant is assigned to a 9-layer graphite exfoliated into an 8- and 1-layer for a Stage-2 expanded graphite shown in Fig. 4c and Supplementary Section S7. Note that the model predicts that trilayer (Fig. 4e) and bilayer (Fig. 4f) graphene are both enriched with mild sonication conditions (short dimensionless time $kt < 0.5$). At the specific dimensionless time, $0.055kt$, the calculated trilayer (35%, Fig. 4e right) and bilayer (40%, Fig. 4f right) graphene concentrations are quantitatively consistent with experimentally observed values using Stage-3 and Stage-2 GICs as the raw materials, respectively. Therefore, by introducing proper graphite materials with a selective laminar structure around a specific layer, as well as mild sonications, the produced solution should be able to reflect the original composition of crystallites directly and form layer-controlled dispersions.

Electronic properties of bi- and trilayer graphene flakes

The large flakes isolated in this work enabled the fabrication of field-effect transistor (FET) devices using conventional ultraviolet photolithography. Several top-gate devices were fabricated (details on device fabrication can be found in Supplementary Section S6). Figure 5a shows a top-view image of the graphene device. Figure 5b–f presents the electronic characterization data of representative bilayer and trilayer devices in the presence of a perpendicular electric field. All measurements were carried out under ambient conditions. The 2D resistivities (the resistance of each device normalized by its channel length and width) of the graphene flakes at zero gate bias are about 1 kΩ, which is one order of magnitude lower than the one corresponding to a film of pristine graphene dispersions[24], and three orders of magnitude lower than the one corresponding to reduced graphene oxide[18,51]. The transfer characteristics show an ambipolar behaviour, and the calculated hole mobility is ∼400 cm^2 V^{-1} s^{-1}. This value is ∼3–7 times lower than that from micromechanically cleaved bilayer and few-layer graphene (∼1,500–3000 cm^2 V^{-1} s^{-1})[52] on a SiO$_2$ substrate, a little bit lower than CVD deposited bilayer graphene (580 cm^2 V^{-1} s^{-1})[10], but ∼1–5 orders of magnitude higher than that from reduced

monolayer graphene oxide (∼0.01–12 cm^2 V^{-1} s^{-1})[18,51,53,54], as shown in Fig. 5b. A number of factors limit our mobility. The extraordinary mobility of monolayer graphene has only been observed on suspended graphene samples at low temperatures[1], and supported graphene has limited mobility due to the scattering effects of the underlying substrate that are still under investigation[56]. In addition, scattering and doping from adsorbed impurities (e.g. oxygen[57], surfactant and photoresist) on graphene surfaces could reduce mobility[58]. We also found that the appearance of the Dirac point and the mobilities of graphene FET devices strongly depend on the photoresist lift-off process. For some of our fabricated devices, we did not observe the Dirac point, and the electronic characteristics showed unipolar behaviour (Supplementary Fig. S12). Figure 5d presents a two-dimensional contour plot of 2D resistivities of a trilayer graphene device as a function of top-gate voltage (V_{TG}) and bottom-gate voltage (V_{BG}). It is encouraging that the resistivity decreases with increasing perpendicular electric field, as observed in ABA-stacked trilayer graphene[4]. The unique electronic properties suggest that the graphene flake is ABA-trilayer. On the other hand, for our bilayer device (Fig. 5f), the Dirac point moves along the diagonal, and the 2D resistivities reach a maximum at the upper-left and lower-right corners. This behaviour is a clear signature of bilayer graphene[55].

Conclusions

We have illustrated an advanced concept for the layer-controlled production of pristine large-area graphene dispersions. The use of ionic graphite intercalation compounds to produce Stage-2 and Stage-3 GICs using ICl and IBr as the ionic intercalants have been shown to be excellent precursors for the production of bilayer and trilayer graphene dispersions. When combined with an on-chip separation method, a population of large-area graphene flakes is produced, such that conventional photolithography is enabled for top-gate device fabrication. Our present approach comprises the only viable route (at this time) to producing AB-stacked bi- and trilayer graphene on arbitrary substrates on a large scale, and the measured mobility values for the devices produced in the present work are the highest for any solution-dispersed material to date. The changes in 2D resistivities of our trilayer and bilayer devices as functions of V_{TG} and V_{BG} exhibit the same characteristics as observed for the case of micromechanically exfoliated graphene.

References
1. Geim, A. K. & Novoselov, K. S. The rise of graphene. *Nature Mater.* **6**, 183–191 (2007).
2. Ohta, T. *et al.* Controlling the electronic structure of bilayer graphene. *Science* **313**, 951–954 (2006).
3. Zhang, Y. B. *et al.* Direct observation of a widely tunable bandgap in bilayer graphene. *Nature* **459**, 820–823 (2009).
4. Craciun, M. F. *et al.* Trilayer graphene is a semimetal with a gate-tunable band overlap. *Nature Nanotech.* **4**, 383–388 (2009).
5. Zhou, S. Y. *et al.* Substrate-induced bandgap opening in epitaxial graphene. *Nature Mater.* **6**, 916–916 (2007).
6. Novoselov, K. S. *et al.* Two-dimensional atomic crystals. *Proc. Natl Acad. Sci. USA* **102**, 10451–10453 (2005).
7. Berger, C. *et al.* Ultrathin epitaxial graphite: 2D electron gas properties and a route toward graphene-based nanoelectronics. *J. Phys. Chem. B* **108**, 19912–19916 (2004).
8. Sutter, P. W., Flege, J. I. & Sutter, E. A. Epitaxial graphene on ruthenium. *Nature Mater.* **7**, 406–411 (2008).
9. Reina, A. *et al.* Large area, few-layer graphene films on arbitrary substrates by chemical vapor deposition. *Nano Lett.* **9**, 30–35 (2009).
10. Lee, S., Lee, K. & Zhong, Z. H. Wafer scale homogeneous bilayer graphene films by chemical vapor deposition. *Nano Lett.* **10**, 4702–4707 (2010).
11. Castro Neto, A. H., Guinea, F., Peres, N. M. R., Novoselov, K. S. & Geim, A. K. The electronic properties of graphene. *Rev. Mod. Phys.* **81**, 109–162 (2009).
12. dos Santos, J. M. B. L., Peres, N. M. R. & Castro, A. H. Graphene bilayer with a twist: electronic structure. *Phys. Rev. Lett.* **99**, 256802 (2007).

13. Coleman, J. N. Liquid-phase exfoliation of nanotubes and graphene. *Adv. Funct. Mater.* **19,** 3680–3695 (2009).
14. Park, S. & Ruoff, R. S. Chemical methods for the production of graphenes. *Nature Nanotech.* **4,** 217–224 (2009).
15. Niyogi, S. *et al.* Solution properties of graphite and graphene. *J. Am. Chem. Soc.* **128,** 7720–7721 (2006).
16. Stankovich, S. *et al.* Synthesis of graphene-based nanosheets via chemical reduction of exfoliated graphite oxide. *Carbon* **45,** 1558–1565 (2007).
17. Li, D., Muller, M. B., Gilje, S., Kaner, R. B. & Wallace, G. G. Processable aqueous dispersions of graphene nanosheets. *Nature Nanotech.* **3,** 101–105 (2008).
18. Tung, V. C., Allen, M. J., Yang, Y. & Kaner, R. B. High-throughput solution processing of large-scale graphene. *Nature Nanotech.* **4,** 25–29 (2009).
19. Wang, S. *et al.* High mobility, printable, and solution-processed graphene electronics. *Nano Lett.* **10,** 92–98 (2010).
20. Gomez-Navarro, C. *et al.* Atomic structure of reduced graphene oxide. *Nano Lett.* **10,** 1144–1148 (2010).
21. Bagri, A. *et al.* Structural evolution during the reduction of chemically derived graphene oxide. *Nature Chem.* **2,** 581–587 (2010).
22. Becerril, H. A. *et al.* Evaluation of solution-processed reduced graphene oxide films as transparent conductors. *ACS Nano* **2,** 463–470 (2008).
23. Blake, P. *et al.* Graphene-based liquid crystal device. *Nano Lett.* **8,** 1704–1708 (2008).
24. Hernandez, Y. *et al.* High-yield production of graphene by liquid-phase exfoliation of graphite. *Nature Nanotech.* **3,** 563–568 (2008).
25. Shih, C. J., Lin, S., Strano, M. S. & Blankschtein, D. Understanding the stabilization of liquid-phase-exfoliated graphene in polar solvents: molecular dynamics simulations and kinetic theory of colloid aggregation. *J. Am. Chem. Soc.* **132,** 14638–14648 (2010).
26. Lotya, M. *et al.* Liquid phase production of graphene by exfoliation of graphite in surfactant/water solutions. *J. Am. Chem. Soc.* **131,** 3611–3620 (2009).
27. Green, A. A. & Hersam, M. C. Solution phase production of graphene with controlled thickness via density differentiation. *Nano Lett.* **9,** 4031–4036 (2009).
28. Green, A. A. & Hersam, M. C. Emerging methods for producing monodisperse graphene dispersions. *J. Phys. Chem. Lett.* **1,** 544–549 (2010).
29. Dresselhaus, M. S. & Dresselhaus, G. Intercalation compounds of graphite. *Adv. Phys.* **30,** 139–326 (1981).
30. Chung, D. D. L. Graphite. *J. Mater. Sci.* **37,** 1475–1489 (2002).
31. Li, X. L. *et al.* Highly conducting graphene sheets and Langmuir–Blodgett films. *Nature Nanotech.* **3,** 538–542 (2008).
32. Ang, P. K., Wang, S. A., Bao, Q. L., Thong, J. T. L. & Loh, K. P. High-throughput synthesis of graphene by intercalation — exfoliation of graphite oxide and study of ionic screening in graphene transistor. *ACS Nano* **3,** 3587–3594 (2009).
33. Lee, J. H. One-step exfoliation synthesis of easily soluble graphite and transparent conducting graphene sheets. *Adv. Mater.* **21,** 4383–4387 (2009).
34. Li, X. L., Wang, X. R., Zhang, L., Lee, S. W. & Dai, H. J. Chemically derived, ultrasmooth graphene nanoribbon semiconductors. *Science* **319,** 1229–1232 (2008).
35. Behabtu, N. *et al.* Spontaneous high-concentration dispersions and liquid crystals of graphene. *Nature Nanotech.* **5,** 406–411 (2010).
36. Zheng, J. A. *et al.* High quality graphene with large flakes exfoliated by oleyl amine. *Chem. Commun.* **46,** 5728–5730 (2010).
37. Lee, J. H. *et al.* The superior dispersion of easily soluble graphite. *Small* **6,** 58–62 (2010).
38. Loh, K. P., Bao, Q. L., Ang, P. K. & Yang, J. X. The chemistry of graphene. *J. Mater. Chem.* **20,** 2277–2289 (2010).
39. Sasa, T., Takahash, Y. & Mukaibo, T. Crystal structure of graphite bromine lamellar compounds. *Carbon* **9,** 407–416 (1971).
40. Daumas, N. & Herold, A. Relations between phase concept and reaction mechanics in graphite insertion compounds. *Comptes Rendus Hebdomadaires Des Seances De L Academie Des Sciences Serie C* **268,** 373–382 (1969).
41. Nikitin, Y. A. & Pyatkovskii, M. L. Formation and properties of materials based on thermally expanded graphite. *Powder Metall. Met. Ceram.* **36,** 41–45 (1997).
42. Deegan, R. D. *et al.* Capillary flow as the cause of ring stains from dried liquid drops. *Nature* **389,** 827–829 (1997).
43. Sharma, R., Lee, C. Y., Choi, J. H., Chen, K. & Strano, M. S. Nanometer positioning, parallel alignment, and placement of single anisotropic nanoparticles using hydrodynamic forces in cylindrical droplets. *Nano Lett.* **7,** 2693–2700 (2007).
44. Sharma, R. & Strano, M. S. Centerline placement and alignment of anisotropic nanotubes in high aspect ratio cylindrical droplets of nanometer diameter. *Adv. Mater.* **21,** 60–65 (2009).
45. Shen, X. Y., Ho, C. M. & Wong, T. S. Minimal size of coffee ring structure. *J. Phys. Chem. B* **114,** 5269–5274 (2010).
46. Sangani, A. S., Lu, C. H., Su, K. H. & Schwarz, J. A. Capillary force on particles near a drop edge resting on a substrate and a criterion for contact line pinning. *Phys. Rev. E* **80,** 011603 (2009).
47. Ferrari, A. C. *et al.* Raman spectrum of graphene and graphene layers. *Phys. Rev. Lett.* **97,** 187401 (2006).
48. De Marco, P. *et al.* Rapid identification of graphene flakes: alumina does it better. *Nanotechnology* **21,** 255703 (2010).
49. Ghosh, D., Gangwar, R. & Chung, D. D. L. Superlattice ordering in graphite-IC1 single-crystals and fibers. *Carbon* **22,** 325–333 (1984).
50. Dotson, N. A. *Polymerization Process Modeling,* xvi, 371 p. (VCH, 1996).
51. Eda, G., Fanchini, G. & Chhowalla, M. Large-area ultrathin films of reduced graphene oxide as a transparent and flexible electronic material. *Nature Nanotech.* **3,** 270–274 (2008).
52. Nagashio, K., Nishimura, T., Kita, K. & Toriumi, A. Mobility variations in mono- and multi-layer graphene films. *Appl. Phys. Exp.* **2,** 025003 (2009).
53. Su, C. Y. *et al.* Electrical and spectroscopic characterizations of ultra-large reduced graphene oxide monolayers. *Chem. Mater.* **21,** 5674–5680 (2009).
54. Gomez-Navarro, C. *et al.* Electronic transport properties of individual chemically reduced graphene oxide sheets. *Nano Lett.* **7,** 3499–3503 (2009).
55. Wang, F. *et al.* Direct observation of a widely tunable bandgap in bilayer graphene. *Nature* **459,** 820–823 (2009).
56. Bruna, M., Vaira, A., Battiato, A., Vittone, E. & Borini, S. Graphene strain tuning by control of the substrate surface chemistry. *Appl. Phys. Lett.* **97,** 021911 (2010).
57. Gunlycke, D., Li, J., Mintmire, J. W. & White, C. T. Altering low-bias transport in zigzag-edge graphene nanostrips with edge chemistry. *Appl. Phys. Lett.* **91,** 112108 (2007).
58. Adam, S., Hwang, E. H., Galitski, V. M. & Das Sarma, S. A self-consistent theory for graphene transport. *Proc. Natl Acad. Sci. USA* **104,** 18392–18397 (2007).

Acknowledgements

Author contributions

C.J.S, A.V., R.K. and M.S.S. conceived and designed the dispersion experiments. C.J.S. and R.K. implemented the dispersion method. C.J.S., A.V., R.S., G.P. and M.H.H. fabricated FET devices. C.J.S. and M.S.S. developed the mathematical model. A.V., R.S., Z.J. and J.H.H. performed the TEM and AFM analysis. C.J.S. performed the XRD and Raman analysis. Q.H.W., S.L. and N.F.R. did additional experiments for revising the manuscript. C.J.S., D.B. and M.S.S. wrote the manuscript with input from A.V. All authors discussed the results and commented on the manuscript.

Additional information